Research Square

Preprints are preliminary reports that have not undergone peer review.
They should not be considered conclusive, used to inform clinical practice,
or referenced by the media as validated information.

Visualization of Long-Range Order in Self-Assembled Ion Barriers for Stable Perovskite Tandems

Tianshi Qin

qintianshi@msn.com

Nanjing Tech University (NanjingTech) https://orcid.org/0000-0002-2084-3537

Wenjian Yan

Nanjing Tech University

You Liu

Anhui Science and Technology University https://orcid.org/0000-0002-3208-5921

Yajun Gao

LONGi Central R&D Institute, LONGi Green Energy Technology Co., Ltd., Xi'an, China

Zhen Xu

Nanjing Tech University

Bingxu Liu

Sun Yat-sen University

Ying Chu

Nanjing Tech University

Yanchen Wang

Henan Institute of Flexible Electronics

Jingxi Chang

Henan Institute of Flexible Electronics

Jinzheng Zhao

Sun Yat-sen University

Xiaopeng Hu

Nanjing Tech University

Jiankai Xie

Sun Yat-sen University

Min Ye

Nanjing Tech University

Si Chen

Nanjing Tech University

Aifei Wang

Nanjing Tech University (NanjingTech)

Jingjin Dong

Nanjing Tech University (NanjingTech) https://orcid.org/0000-0002-2406-504X

Jiupeng Cao

Nanjing Tech University (NanjingTech)

Chengrong Yin

Nanjing Tech University

Bo He

LONGi Central R&D Institute, LONGi Green Energy Technology Co., Ltd. https://orcid.org/0009-0008-0762-7419

Wei Huang

Northwestern Polytechnical University https://orcid.org/0000-0001-7004-6408

Article

Keywords:

Posted Date: June 1st, 2026

DOI: https://doi.org/10.21203/rs.3.rs-9404112/v1

License: This work is licensed under a Creative Commons Attribution 4.0 International License. Read Full License

Additional Declarations: There is **NO** Competing Interest.

Abstract

The arrangement of self-assembled molecules on perovskite surfaces has remained a black box, despite their widespread use across perovskite optoelectronics. All prior understanding has relied on computational simulations that default to random or short-range ordered packing. Here we report the direct visualization of this arrangement at atomic resolution. Scanning tunnelling microscopy reveals that a fully conjugated, planar molecule assembles into regularly repeating arrays of hundreds of molecular units, and complementary techniques confirm that this long-range order is conformally preserved on perovskite surfaces, including the textured silicon in tandems. This nearly square packing aligns with the cubic perovskite lattice and matches grain dimensions, enabling uniform coating. Four carbonyl groups, one at each corner of the molecule, form intermolecular coordination bonds that encircle each molecular unit, creating a supramolecular network that locks the ordered configuration while blocking metal ion migration. Incorporated into perovskite/silicon tandem solar cells, this self-assembled ion barrier achieves a power conversion efficiency exceeding 34.5% (certified steady-state 34.4%) and retains its performance under continuous illumination, light-dark cycling, damp-heat exposure, and thermal shock. The extracted structural parameters, including molecular orientation, intermolecular spacing, π-π stacking periodicity, and lamellar packing distances, provide an experimental benchmark to calibrate future simulations across the field.

Introduction

Self-assembled molecules (SAMs) have emerged as transformative components in perovskite (PSK) optoelectronics, playing a pivotal role in the recent performance leap of inverted perovskite solar cells[1-8]. Despite their widespread adoption, the actual molecular arrangement of these layers on PSK surfaces has remained a black box. Landmark studies have consistently relied on computational simulations or indirect inferences to deduce molecular packing and orientation[9-20], yet the true arrangement has never been directly visualized. Without experimental constraints, all structural models have defaulted to random or short-range ordered configurations. This gap has fundamentally limited rational molecular design: without knowing how molecules pack, functional group positions and intermolecular interactions cannot be precisely engineered.

Here we provide the first direct visualization of self-assembled molecular arrangement at atomic resolution. By combining scanning tunnelling microscopy (STM) on atomically flat substrates with complementary techniques that probe molecular packing on rough surfaces, we reveal the arrangement of 3,4,9,10-perylenetetracarboxylic dianhydride (PTCDA), a fully conjugated, planar molecule that can be thermally evaporated conformally onto PSK films, including the textured silicon substrates essential for tandem solar cells. STM images show that PTCDA assembles into regularly repeating arrays of hundreds of molecular units, establishing long-range order that is conformally preserved on PSK surfaces. The packing adopts a nearly square geometry that aligns with the cubic PSK lattice and matches grain dimensions, enabling uniform coating.

Guided by this structural insight, we exploit the square packing for precision molecular engineering. Four carbonyl groups, one at each corner of the PTCDA molecule, are positioned by the ordered lattice to form intermolecular coordination bonds that encircle each molecular unit. This creates a supramolecular network, which we term a self-assembled ion barrier (SAIB), that locks the ordered configuration while blocking metal ion migration. Incorporated into perovskite/silicon tandem solar cells, the SAIB achieves a power conversion efficiency of 34.58% (certified 34.49%) and retains its performance under continuous illumination, light-dark cycling, damp-heat exposure, and thermal shock. The extracted structural parameters, including molecular orientation, intermolecular spacing, π-π stacking periodicity, and lamellar packing distances, provide an experimental benchmark to calibrate future simulations across the field.

Main

Direct Visualization of Long-Range Molecular Order

The molecular arrangement of SAMs on photovoltaic-relevant surfaces has been studied exclusively through computational simulations. Without experimental constraints, these models invariably default to random or short-range ordered configurations[1-20]. To determine the actual packing geometry, we performed STM on atomically flat Ag(111) substrates[21]. We selected PTCDA because its planar, conjugated architecture permits thermal evaporation directly onto PSK surfaces (Supplementary Fig. 1), including the textured silicon substrates of tandem devices. As a benchmark, we also examined C_{60}, a spherical molecule widely used in PSK photovoltaics.

STM images revealed a striking difference between the two systems. C_{60} assembled into a honeycomb lattice (Fig. 1a), consistent with prior reports on metal substrates[22]. PTCDA organized into regularly repeating arrays with a nearly square geometry (Fig. 1b). Fast Fourier transform (FFT) analysis of both images yielded well-defined diffraction spots (Fig. 1a,b insets), confirming long-range periodicity in reciprocal space[23]. From the FFT patterns and direct STM measurements, the intermolecular spacing of PTCDA was determined to be approximately 11.5 Å, with both methods yielding consistent values. The ordered domains extended without interruption across the entire imaging field, encompassing hundreds of molecular units, establishing long-range order over length scales exceeding several hundred nanometres (Supplementary Fig. 2).

These structural parameters enabled us to construct physically realistic repeating units of both molecular layers on the formamidinium lead iodide ($FAPbI_3$) (100) surface (Fig. 1c). Triangularly packed C_{60} exhibited pronounced symmetry breaking from lattice mismatch, with bond length deviations up to 1.4 Å. Square-packed PTCDA showed much weaker deviations of only 0.7 Å. Adsorption energy calculations further demonstrated that PTCDA binds substantially more strongly (–2.25 eV) than C_{60} (–0.59 eV), consistent with multidentate carbonyl coordination to surface Pb sites[24].

We used grazing-incidence wide-angle X-ray scattering (GIWAXS) to examine the vertical packing (Fig. 1d, Supplementary Fig. 3 and Supplementary Table 1)[25]. C_{60} showed a primary diffraction peak at 0.77 $Å^{-1}$, corresponding to a d-spacing of approximately 8.1 Å. PTCDA exhibited its highest peak at 1.98 $Å^{-1}$, yielding a d-spacing of approximately 3.2 Å, characteristic of π–π stacking in planar conjugated systems. This marked reduction confirms that PTCDA packs substantially more densely than C_{60}.

To assess the functional consequences of this dense packing, we turned to X-ray photoelectron spectroscopy (XPS) and Auger electron spectroscopy (AES)[26]. At the Ag interface (Fig. 1e), PTCDA strongly attenuated the Ag^+ signal, reducing the Ag^+/total Ag ratio from 15.21% for pristine Ag to 1.30%, compared to 9.63% with C_{60} (Supplementary Table 2). At the PSK interface (Fig. 1f), PTCDA caused a clear positive shift in Pb *4f* binding energy. The Pb^0 content dropped from 20.12% in pristine PSK to undetectable levels, whereas C_{60} reduced it only to 3.96% (Supplementary Table 3). The I *3d* peak remained stable (Supplementary Fig. 4), indicating preferential interaction with Pb^{2+} sites through carbonyl groups. AES elemental mapping of 2 nm-thick films on Ag (Fig. 1g, Supplementary Fig. 5,6) showed exposed Ag atom ratios of approximately 35% for PTCDA versus 65% for C_{60}, a direct consequence of the denser packing afforded by the planar architecture.

Taken together, these results establish that PTCDA forms a densely packed, ordered molecular layer with strong coordination affinity for metal ions. The structural parameters extracted from STM and GIWAXS, which include square packing geometry, 11.5 Å intermolecular spacing, and 3.1 Å π–π stacking distance, provide a quantitative basis for molecular engineering of an ion barrier.

A Coordinative Network Encircles Each Molecule as an Ion Barrier

The long-range ordering revealed by STM places the four carbonyl groups of each PTCDA molecule at the corners of a nearly square lattice. Adjacent carbonyls are brought into close proximity, forming intermolecular coordination bonds that encircle each molecular unit in a continuous supramolecular network. We term this a self-assembled ion barrier (SAIB), because the network is structurally poised to capture metal ions attempting to penetrate the layer.

We tested this concept by mapping Ag^+ distribution in full devices after 72 hours of maximum power point tracking. Devices with the architecture glass/indium tin oxides (ITO)/[4-(3,6-Dimethoxy-9H-carbazol-9-yl)butyl]phosphonic acid (MeO-4PACz)/PSK/SAIB (with and without)/C_{60}/bathocuproine (BCP)/Ag were analysed by correlative time-of-flight secondary ion mass spectrometry (TOF-SIMS) and scanning electron microscopy (SEM) (Fig. 2a,b)[27]. In the device without SAIB, Ag^+ ions migrated from the electrode through the C_{60} layer and accumulated extensively within the PSK. Depth-resolved profiles and in-plane slices at five depths revealed pronounced Ag^+ penetration, with grain boundary enrichment clearly visible at 400 and 600 nm depths. In the device with SAIB, Ag^+ was effectively confined above the PSK. Slices corresponding to the PSK region showed near-background Ag^+ signals, while SEM images

confirmed identical morphologies between the two samples (Supplementary Fig. 7–10). The SAIB therefore blocks extrinsic ion ingress without altering device morphology.

To resolve the barrier mechanism, we modelled the C_{60}/PSK and PTCDA/PSK interfaces using the triangular and square lattices determined experimentally by STM (Fig. 2c,d). Energy barrier calculations for Ag^+ migration followed a Lennard-Jones-type potential profile (Supplementary Fig. 11)[28]. The C_{60} layer presented a peak energy barrier of only 0.86 eV, consistent with weak van der Waals interactions between C_{60} and Ag^+. The PTCDA layer exhibited a substantially higher barrier of 1.78 eV. This difference arises from the square packing geometry. When an Ag^+ ion traverses the central region formed by four adjacent PTCDA molecules, it encounters four inwardly directed carbonyl groups. The ion becomes coordinated by these carbonyls, with Ag–O distances of 2.3–2.6 Å, creating an effective trapping site that blocks further penetration.

Fourier transform infrared (FTIR) measurements confirmed this coordination chemistry (Fig. 2e)[29]. Upon exposure to Ag^+, the C=O stretching vibration of PTCDA at 1773 cm^{-1} shifted to 1757 cm^{-1}, while the conjugated C=C stretching peak at 1595 cm^{-1} remained unchanged. The C=C bond therefore serves as a negative control, confirming that Ag^+ interacts specifically with the carbonyl groups rather than with the aromatic framework. Combined with the XPS and AES results, these data establish that the square packing positions four carbonyl groups to form a coordination cage around each molecular unit. This supramolecular network simultaneously stabilizes the molecular packing and captures metal ions that attempt to cross the SAIB.

A Universal Conformal Strategy Across Device Architectures

To evaluate whether the SAIB can be applied to the textured substrates required for tandem devices, we fabricated perovskite/silicon tandem cells with the architecture heterojunction silicon (HJT-Si)/indium zinc oxide (IZO)/MeO-4PACz/PSK/SAIB (with and without)/C_{60}/SnO_2/IZO/Ag (Fig. 3a). Cross-sectional SEM imaging confirmed that despite the nearly 150 nm height variation of the PSK surface atop textured silicon, the SAIB, C_{60}, and SnO_2 layers each deposited as continuous, conformal films (Fig. 3b).

We verified the coverage uniformity of the SAIB layer using photoinduced force microscopy (PiFM)[30]. The sample with SAIB exhibited a uniform PTCDA characteristic signal at 1595 cm^{-1} across the entire scanned region, whereas the PSK without SAIB surface showed only the FA peak at 1714 cm^{-1} (Fig. 3c). The thin conformal coating preserved the underlying surface morphology without observable changes (Fig. 3d, Supplementary Fig. 12). In-situ photoinduced infrared (PiIR) spectroscopy provided depth-resolved chemical profiling (Fig. 3e, Supplementary Fig. 13). The surface spectrum displayed peaks at 1024 cm^{-1} (aromatic C–H in-plane bending), 1595 cm^{-1} (aromatic C=C skeletal vibration), 1264 and 1302 cm^{-1} (anhydride C–O–C stretch), and 1773 cm^{-1} (symmetric C=O stretch), all characteristic of PTCDA. With increasing PiIR penetration depth, the FA-related C=N stretch at 1714 cm^{-1} intensified,

while the PTCDA-derived peaks gradually attenuated, confirming the expected stratification of the SAIB layer atop the PSK.

We optimized the SAIB thickness using single-junction devices with SAIB layers of 1, 2, and 3 nm (Supplementary Fig. 14 and Supplementary Tables 4–7), identifying 2 nm as the optimal thickness. Under these conditions, the champion tandem device achieved a power conversion efficiency (*PCE*) of 34.58%, with an open-circuit voltage (V_{OC}) of 2.00 V, a short-circuit current density (J_{SC}) of 20.37 mA cm^{-2}, and a fill factor (*FF*) of 84.57% (Fig. 3f). The PSK subcell exhibited a *PCE* of 23.40% (V_{OC} = 1.26 V, J_{SC} = 21.84 mA cm^{-2}, *FF* = 84.57%), and the HJT-Si subcell delivered a *PCE* of 24.61% (V_{OC} = 0.71 V, J_{SC} = 41.11 mA cm^{-2}, *FF* = 83.88%) (Fig. 3g, Supplementary Fig. 16 and Supplementary Table 8,9). The certified steady-state efficiency measured by maximum power point tracking (MPPT) at the National Renewable Energy Laboratory reached 34.49% with a maximum power output of 34.68 mW, maintained for over 600 seconds (Supplementary Fig. 15). External quantum efficiency (EQE) spectra yielded integrated current densities of 21.04 mA cm^{-2} and 20.33 mA cm^{-2} for the PSK and HJT-Si subcells, respectively, consistent with the measured J_{SC} values (Fig. 3h).

The conformal evaporation process is not limited to tandem architectures. The same protocol was applied directly to planar single-junction devices without any modification, and the SAIB layer delivered equivalent performance gains (Supplementary Tables 4–7). This substrate independence follows directly from the nature of vacuum deposition: having demonstrated uniform coverage on the most challenging surface, the textured silicon in tandems, application to planar architectures is straightforward. The SAIB strategy is therefore relevant across the PSK optoelectronics platform.

Resolving the Efficiency Rise-and-Decay Phenomenon

Under ISOS-L-1 conditions (continuous 1-sun illumination, 25 °C), the device with SAIB retained 96% of its initial efficiency after 2,000 hours, compared to 77% for the device without SAIB (Fig. 4a). Under ISOS-LC-1 light-dark cycling (24 h period, 1:1 duty cycle), the device with SAIB maintained 98% after 60 cycles, while the device without SAIB dropped to 82% (Fig. 4b).

Examination of the MPPT data revealed a notable pattern (Fig. 4a, inset). In the device without SAIB, PCE increased gradually over the first 72 hours, then entered a pronounced decay. This initial rise followed by continuous decline is widely observed in PSK devices but has remained mechanistically unresolved[31-34]. In the device with SAIB, the post-rise decay was arrested, with PCE remaining nearly stable after 72 hours.

To determine the mechanism, we tracked electron mobility (μ_e)[35], trap density (N_t)[36], and carrier lifetime (τ_{ave})[37] under illumination. μ was measured by SCLC in electron-only devices (glass/ITO/Ag/SAIB (with and without)/C_{60}/Ag, Fig. 4c). In the device without SAIB, μ rose from 1.0×10^{-4} to 1.2×10^{-4} cm^2 V^{-1} s^{-1} within 72 hours before stabilizing; the device with SAIB showed a similar increase from 1.1×10^{-4}

to 1.3×10^{-4} cm^2 V^{-1} s^{-1}. These trends indicate that Ag^+ migration from the electrode into C_{60} enhances μ_e through a doping effect until saturation (Supplementary Fig. 17–19, Table 10). The SAIB itself maintained a stable μ of ~8.0×10^{-5} cm^2 $V^{-1}s^{-1}$, consistent with a tunnelling barrier.

N_t was evaluated in devices with the structure glass/ITO/SnO_2/PSK/SAIB (with and without)/C_{60}/Ag (Fig. 4d). Under 120 hours of illumination, N_t in the device without SAIB increased from 2.0×10^{15} to 3.0×10^{15} cm^{-3}, attributed to Ag^+ penetration into PSK. In the device with SAIB, N rose only from 1.9×10^{15} to 2.2×10^{15} cm^{-3} within 72 hours before stabilizing (Supplementary Fig. 20,21, Table 11).

TRPL measurements on glass/PSK/SAIB (with and without)/C_{60}/AgI stacks (Fig. 4e) showed that τ_{ave} of a neat PSK film fell sharply from ~220 ns to 22 ns after 120 hours. In the device without SAIB, τ_{ave} dropped from ~80 ns to 36 ns. In the device with SAIB, τ_{ave} declined more gradually, from ~75 ns to a stabilized ~53 ns (Supplementary Fig. 22–24, Table 12).

These three measurements converge on a single mechanism. Initially, Ag^+ migrates into C_{60}, doping the layer and raising μ, producing a temporary *PCE* rise. Continued migration drives Ag^+ into PSK, increasing N and non-radiative recombination, causing the subsequent decay. The SAIB interrupts this cycle by confining Ag^+ above the PSK. Mobility enhancement in C_{60} still occurs, but ions are blocked before degrading the perovskite, locking in peak performance.

The SAIB also functions as an internal moisture barrier, with water contact angle increasing from 54° to 74° (Fig. 4f). Under damp-heat (85 °C/85% RH, ISOS-D-3, 1,500 h), the device with SAIB retained 92% of initial PCE versus 79% without (Fig. 4g). Under thermal cycling (−40 to 85 °C, ISOS-T-3, 200 cycles), the device with SAIB retained 96% versus 90% without (Fig. 4h).

Conclusion

We have directly visualized the molecular arrangement of a self-assembled layer on a photovoltaic-relevant surface, resolving a long-standing structural mystery in perovskite optoelectronics. STM reveals that PTCDA assembles into highly ordered arrays with long-range periodicity over several hundred nanometres. The nearly square packing geometry aligns with the cubic perovskite lattice and matches grain dimensions, enabling uniform coating. In this configuration, four carbonyl groups sit at the corners of each molecular unit, forming a coordinative network that encircles each molecule. The resulting self-assembled ion barrier blocks metal ion migration while stabilizing the molecular packing. Using this near-perfect ion-blocking platform, we resolved the mechanistic origin of the widely observed efficiency rise-and-decay phenomenon, demonstrating that it is driven by ion migration into the perovskite and that suppressing this migration locks devices in their peak-performance state. The conformal evaporation process is substrate-independent, requiring no modification across different device architectures. The extracted structural parameters provide an experimental benchmark to calibrate future computational simulations. We expect these findings to open new directions in the rational design of self-assembled

molecular layers, where long-range order becomes a design parameter that can be systematically exploited.

Methods

Materials

[3,4,9,10-Perylenetetracarboxylic dianhydride] (PTCDA, purified by sublimation >98.0%), [4-(3,6-dimethoxy-9H-carbazol-9-yl)butyl]phosphonic acid (MeO-4PACz, >98.0%), ethylenediamine dihydroiodide (EDAI, >98.0%), fullerene (C_{60}, purified by sublimation >99.5%), bathocuproine (BCP, purified by sublimation >99.0%), lead(II) iodide (PbI_2, 99.99%), and lead(II) bromide ($PbBr_2$, >99.0%) were purchased from TCI. Formamidinium iodide (FAI, ≥99.9%) was purchased from Greatcell Solar Materials. Methylammonium bromide (MABr, ≥99.5%) and cesium iodide (CsI, >99.5%) were purchased from were purchased from Xi'an Polymer Light Technology Corp. Dimethyl sulfoxide (DMSO, anhydrous, ≥99.9%), dimethylformamide (DMF, anhydrous, ≥99.9%), ethanol (anhydrous, ≥99.9%), ethyl acetate (anhydrous, ≥99.8%) and 2-propanol (anhydrous, ≥99.8%) were purchased from Sigma Aldrich.

Methods for HJT-Si bottom cells

The n-type Czochralski silicon wafer was utilized to prepare the silicon bottom cell. The wafers were initially cleaned, removing surface impurities, followed by a chemical polishing to remove the surface slicing damage. Subsequently, the rear surface of the wafers underwent treatment with a standard texturing process to produce 3–5-μm pyramids, and the front side was textured with a pyramid size of 0.5–1 μm using a relatively low alkaline concentration. After the texturing process, hydrogenated intrinsically amorphous (i-a-Si:H) layers were formed on both sides of the Czochralski wafers. Sequentially, n-type nanocrystalline silicon oxide (nc-SiOx:H) and p-type nc-Si:H layers were deposited on the front and rear sides of the silicon substrate through plasma-enhanced chemical vapour deposition, respectively. A 100-nm-thick In_2O_3-based IZO film was stacked on the back side of the substrate, followed by the silver (Ag) electrodes onto the IZO layer. Furthermore, approximately 10-nm-thick IZO film was deposited on the nc-SiO_x:H as the recombination layer. Finally, the prepared silicon bottom cells were cut into 2.03 × 2.03 cm^2 substrates by a laser-cutting technique.

Methods for PSK/Si tandem cells

HJT-Si bottom cells were transferred into a nitrogen-filled glovebox for tandem cell fabrications. MeO-4PACz (1 mg mL^{-1} in ethanol) was spin-coated at 3,000 rpm for 30 s and annealed at 100 °C for 10 min. A triple-cation wide-bandgap PSK precursor solution (1.53 M) with a composition of $Cs_{0.02}(FA_{0.77}MA_{0.23})_{0.98}Pb(I_{0.77}Br_{0.23})_3$ and 4.5% excess $PbBr_2$ was prepared by dissolving CsI, FAI, MABr, PbI_2 and $PbBr_2$ in a mixed solvent of DMF and DMSO (4:1, v/v), followed by overnight stirring at room temperature. Prior to use, the solution was filtered through a 0.22 μm polytetrafluoroethylene membrane. The PSK film was deposited via a two-step spin-coating process: 1,000 rpm for 15 s,

followed by 3,500 rpm for 40 s, with 200 μL of ethyl acetate dropped during the final 10 s. The film was then annealed at 100 °C for 30 min. Subsequently, an EDAI passivation layer (0.5 mg ml^{-1} in 2-propanol) was spin-coated onto the PSK film at 4,000 rpm for 20 s. Afterward, PTCDA (2 nm, 0.05 Å s^{-1}) and C_{60} (10 nm, 0.15 Å s^{-1}) were sequentially deposited by thermal evaporation under a pressure of ~10^{-5} torr in a vacuum chamber. A 15 nm SnO_2 layer was then deposited by atomic layer deposition, followed by IZO deposition via radio-frequency magnetron sputtering. Finally, a 700 nm Ag finger electrode was thermally evaporated under a pressure of ~10^{-5} torr through a high-precision shadow mask, and a 110 nm MgF_2 anti-reflection layer was subsequently deposited on whole surface.

Density functional theory (DFT). Spin-polarized density functional theory (DFT) computations were executed within the CP2K software suite[43]. A hybrid Gaussian/plane-wave basis set framework was utilized throughout this study. Core electron interactions were modeled using norm-conserving Goedecker-Teter-Hutter pseudopotentials[44–46], while the valence region was described by a double-zeta polarization basis set coupled with an auxiliary plane-wave basis having a 450 Ry energy cutoff [47]. For the exchange–correlation functional, the Perdew–Burke–Enzerhof (PBE) formulation under the generalized gradient approximation was applied[48]. Geometry optimizations employed the Broyden–Fletcher–Goldfarb–Shanno (BFGS) minimizer, with convergence defined by a self-consistent field energy threshold of 1.0×10^{-5} au. All calculations incorporated van der Waals dispersion corrections via the empirical damped DFT-D3 scheme[49]. To determine migration energy barriers, the climbing-image nudged elastic band (CI-NEB) method[50,51] , was implemented, utilizing seven discretized images along the reaction coordinate connecting the initial and final states.

Efficiency measurements. *J-V* curves were measured under AM 1.5G illumination using a Class 3A solar simulator (XES-40S3, SAN-EI), with the light intensity calibrated by a Newport reference cell. The active area was defined by an aperture shade mask (0.05 cm^2 for single-junction devices). The *J–V* characterizations of the perovskite/silicon TSCs were detected by a Keithley 2400 source measurement unit at 25 °C under AM 1.5G illumination (100 mW cm^{-2}). The simulator illumination intensity was calibrated by using Fraunhofer ISE CalLab certified c-Si solar cells. The *J–V* curves of all devices were measured with a step size of 10 mV and a delay time of 10 ms by using a black mask with an aperture area of about 1.0 cm^2. External quantum efficiency was measured by a Enli Tech system. A green LED light with peak wavelength of 525 nm and a near-infrared LED with peak wavelength of 845 nm were used to measure the silicon bottom subcell and the perovskite top cell (0.5 V bias voltages were applied), respectively.

Stability measurements. The MPP stability tracking test for the ISOS-L-1 protocol involved unencapsulated PSCs stored at 25 ± 2 °C under simulated 1-sun AM 1.5 G illumination in a nitrogen atmosphere. The illumination source is a UV-free white-light LED, with its intensity calibrated to match 1-sun conditions. For the ISOS-L-3 ageing test, the equipment was placed in a constant temperature and humidity chamber set to 85 °C and 85% relative humidity. The dark–light cycling stability measurements

for the ISOS-LC-1 protocol involved exposing PSCs to simulated 1-sun illumination, alternating between light and dark for 24-hour cycles with a 1:1 duty cycle. The 12-hour light/12-hour dark regimen replicates the natural 24-hour diurnal rhythm. The thermal cycling stability of the perovskite films/devices under the ISOS-T-3 protocol was evaluated by repeatedly cycling the temperature between –40 °C and 85 °C. Each cycle consisted of heating from 25 °C to 85 °C at a rate of 10 °C min^{-1}, holding at 85 °C for 3 min, followed by cooling back to –40 °C at the same rate. The samples were subjected to 200 cycles under an ambient N_2 atmosphere. All devices employed for stability measurements were encapsulated.

STM characterizations. The experiments were performed using a Unisoku STM/AFM with a qPlus configuration, operated at low temperature (T ≈ 5 K) and under ultrahigh vacuum (UHV, P ≈ 10^{-10} Torr). The Ag(111) surface was cleaned through repeated cycles of Ar^+ sputtering and annealing. The tungsten tip was covered with layers of Ag atoms after penetrating the Ag(111) substrate. Ultrathin films of PTCDA and C_{60} molecules were generated on the metal substrate by thermal sublimation from tantalum boats. All STM images were processed using the WSxM software[42].

WAXS characterizations. WAXS measurements[43] were conducted using the Xeuss 2.0 small-/wide-angle X-ray scattering system from Xenocs. The instrument employs a copper target X-ray source with a power of 30 W and an X-ray wavelength of 1.5 Å. Scattered signals were collected using a Pilatus 3R 300K detector with a pixel size of 172 μm.

AES characterizations. AES measurements were conducted using the Auger Electron Spectroscopy (PHI 710). Electron gun: Electron beam voltage: 5 kV; Electron beam current: 10 nA.

SEM and TOF-SIMS characterizations. A TOF-SIMS analysis system (Tofwerk AG and Carl Zeiss Microscopy) attached to the Crossbeam540 was used for TOF-SIMS analysis[29,30]. The depth profiling was obtained through a 30 keV Ga^+ ions sputtering beam raster of 8 × 8 μm area. Secondary ions originating from the ion-sample interaction were detected and imaged. The maps showed the spatially distributed secondary ion signal from the TOF-SIMS detector.

PiFM characterizations. PiFM measurements were performed using a Molecular Vista PiFM system (model: PiFM-IR, Molecular Vista, USA). This system utilizes a multi-modal atomic force microscope (AFM) to perform photo-induced force microscopy (PiFM) and spectroscopy (PiF-IR), allowing for high-resolution chemical mapping and topographical imaging. The system captures both PiFM chemical maps and surface topography images simultaneously. The PiFM technique works by detecting force interactions between the AFM tip and the sample induced by laser excitation at selected infrared wavelengths.

Other characterizations. UPS analyses were carried out on a Thermo Fisher Escalab 250xi system. XPS measurements were conducted using a PHI 5000 VersaProbe III (Ulvac-Phi). Curve fitting was performed using the Thermo Avantage software. The curves were corrected based on the C *1s* peak at 284.8 eV. UV-Vis absorption spectra were obtained using a UV-1750 spectrophotometer (Shimadzu). TRPL and

steady-state PL measurements were executed with an FLS980 spectrometer (Edinburgh Instruments). SCLC measurements were recorded using a Keithley 4200 semiconductor parameter analyzer (SMU, Keithley). FTIR spectroscopy was carried out using an INVENIO S spectrometer.

Declarations

Data Availability

All data are available in the main text or the Supplementary Information. Further data are available from the corresponding authors on reasonable request.

Competing interests:

The authors declare no competing interests.

References

1. Park, S. M. et al. Low-loss contacts on textured substrates for inverted perovskite solar cells. *Nature* **624**, 289–294 (2023).
2. Liu, S. et al. Buried interface molecular hybrid for inverted perovskite solar cells. *Nature* **632**, 536–542 (2024).
3. Wang, Y. et al. Homogenized contact in all-perovskite tandems using tailored 2D perovskite. *Nature* **635**, 867–873 (2024).
4. Jia, L. et al. Efficient perovskite/silicon tandem with asymmetric self-assembly molecule. *Nature* **644**, 912–919 (2025).
5. Jiang, W. et al. Toughened self-assembled monolayers for durable perovskite solar cells. *Nature* **646**, 95–101 (2025).
6. Dai, Z. et al. Interfacial toughening with self-assembled monolayers enhances perovskite solar cell reliability. *Science* **372**, 618–622 (2021).
7. Tang, H. et al. Reinforcing self-assembly of hole transport molecules for stable inverted perovskite solar cells. *Science* **383**, 1236–1240 (2024).
8. Yang, Y. et al. Hafnium oxide interface stabilization for efficient, photothermally stable perovskite solar cells. *Science* **391**, 926–930 (2026).
9. Zhang, C. et al. Ti_3–graphene single-atom material for improved energy level alignment in perovskite solar cells. *Nat. Energy* **6**, 1154–1163 (2021).
10. Ying, Z. et al. Antisolvent seeding of self-assembled monolayers for flexible monolithic perovskite/Cu(In,Ga)Se_2 tandem solar cells. *Nat. Energy* **10**, 737–749 (2025).
11. Dong, B. et al. Self-assembled bilayer for perovskite solar cells with improved tolerance against thermal stresses. *Nat. Energy* **10**, 342–353 (2025).

12. Li, T. et al. Quasi-random oriented molecular contacts for inverted perovskite solar cells with improved efficiency. *Nat. Energy* (2026). DOI: 10.1038/s41560-026-02024-7
13. Feng, Q. et al. Amorphous self-assembled multilayers for perovskite solar cells with improved reverse bias stability. *Nat. Energy* (2026). DOI: 10.1038/s41560-026-02015-8
14. Li, M. et al. A molecularly engineered electron-selective self-assembled monolayer enhances quasi-Fermi level splitting in inverted perovskite solar cells. *Nat. Energy* (2026). DOI: 10.1038/s41560-026-02025-6
15. Wang, D. et al. Self-assembled molecules with hydrogen-bond networks enable efficient all-perovskite tandem solar cells. *Nat. Energy* **11**, 436–448 (2026).
16. Wang, X. et al. Regulating phase homogeneity by self-assembled molecules for enhanced efficiency and stability of inverted perovskite solar cells. *Nat. Photon.* **18**, 1269–1275 (2024).
17. Zhang, D. et al. Perovskite crystallization control via an engineered self-assembled monolayer in perovskite–silicon tandem solar cells. *Nat. Photon.* **20**, 40–48 (2026).
18. Gao, D. et al. High-efficiency perovskite solar cells enabled by suppressing intermolecular aggregation in hole-selective contacts. *Nat. Photon.* **19**, 1070–1077 (2025).
19. Tian, C. et al. Photostable donor–acceptor interface for minimizing energy loss in inverted perovskite solar cells. *Nat. Photon.* **20**, 287–295 (2026).
20. Luo, C. et al. Engineering bonding sites enables uniform and robust self-assembled monolayer for stable perovskite solar cells. *Nat. Mater.* **24**, 1265–1272 (2025).
21. Anirban, A. 40 years of scanning tunnelling microscopy. *Nat. Rev. Phys.* **4**, 291 (2022).
22. Feng, M. et al. Atomlike, hollow-core–bound molecular orbitals of C_{60}. *Science* **320**, 359–362 (2008).
23. Cheung, S. C. et al. Dictionary learning in Fourier-transform scanning tunneling spectroscopy. *Nat. Commun.* **11**, 1081 (2020).
24. Jin, L. et al. Suppressing solvent adducts via coordination competition enables scalable perovskite photovoltaics. *Nat. Commun.* **17**, 1737 (2026).
25. Pan, F. et al. Long-range ordered porous carbons produced from C_{60}. *Nature* **614**, 95–101 (2023).
26. Greczynski, G. et al. X-ray photoelectron spectroscopy: Towards reliable binding energy referencing. *Prog. Mater. Sci.* **107**, 100591 (2020).
27. Zhao, J. et al. Impact of lithium dopants in hole-transporting layers on perovskite solar cell stability under day–night cycling. *Nat. Energy* **10**, 1226–1236 (2025).
28. Haruyama, J. et al. First-principles study of ion diffusion in perovskite solar cell sensitizers. *J. Am. Chem. Soc.* **137**, 10048–10051 (2015).
29. Baiz, C. R. et al. Two-dimensional infrared spectroscopy of metal carbonyls. *Acc. Chem. Res.* **42**, 1395–1404 (2009).
30. Nowak, D. et al. Nanoscale chemical imaging by photoinduced force microscopy. *Sci. Adv.* **2**, e1501571 (2016).

31. Lin, Y.-H. et al. A piperidinium salt stabilizes efficient metal-halide perovskite solar cells. *Science* **369,** 96–102 (2020).
32. Lin, R. et al. All-perovskite tandem solar cells with 3D/3D bilayer perovskite heterojunction. *Nature* **620,** 994–1000 (2023).
33. Zhuang, X. et al. Homogenized chlorine distribution for >27% power conversion efficiency in perovskite solar cells. *Science* **390,** 638–642 (2025).
34. Zhang, J. et al. In situ dynamic regulation of strain at the buried interface of stable perovskite solar cells. *Nat. Photonics* **20,** 119–127 (2026).
35. Herz, L. M. Charge-carrier mobilities in metal halide perovskites: Fundamental mechanisms and limits. *ACS Energy Lett.* **2**, 1539–1548 (2017).
36. Shi, D. et al. Low trap-state density and long carrier diffusion in organolead trihalide perovskite single crystals. *Science* **347**, 519–522 (2015).
37. de Quilettes, D. W. et al. Impact of microstructure on local carrier lifetime in perovskite solar cells. *Science* **348**, 683–686 (2015).
38. VandeVondele, J. et al. Quickstep: Fast and accurate density functional calculations using a mixed Gaussian and plane waves approach. *Comput. Phys. Commun.* **167**, 103–128 (2005).
39. Goedecker, S. et al. Separable dual-space Gaussian pseudopotentials. *Phys. Rev. B* **54**, 1703–1710 (1996).
40. Hartwigsen, C. et al. Relativistic separable dual-space Gaussian pseudopotentials from H to Rn. *Phys. Rev. B* **58**, 3641–3652 (1998).
41. Krack, M. et al. All-electron ab initio molecular dynamics. Phys. *Chem. Chem. Phys.* **2**, 2105–2112 (2000).
42. VandeVondele, J. et al. Gaussian basis sets for accurate calculations on molecular systems in gas and condensed phases. *J. Chem. Phys.* **127**, 114105 (2007).
43. Perdew, J. P. et al. Generalized gradient approximation made simple. *Phys. Rev. Lett.* **77**, 3865–3868 (1996); *Erratum Phys. Rev. Lett.* **78**, 1396 (1997).
44. Grimme, S. et al. A consistent and accurate ab initio parametrization of density functional dispersion correction (DFT-D) for the 94 elements H–Pu. *J. Chem. Phys.* **132**, 154104 (2010).
45. Henkelman, G. et al. A climbing image nudged elastic band method for finding saddle points and minimum energy paths. *J. Chem. Phys.* **113**, 9901–9904 (2000).
46. Mills, G. et al. Reversible work transition state theory: Application to dissociative adsorption of hydrogen. *Surf. Sci.* **324**, 305–337 (1995).
47. Horcas, I. et al. WSXM: A software for scanning probe microscopy and a tool for nanotechnology. *Rev. Sci. Instrum.* **78**, 013705 (2007).
48. Huang. J. GIWAXS-Tools, Version (2.4.5), https://gitee.com/swordshinehjy/giwaxs-script. (accessed on January. 2026).

Figures

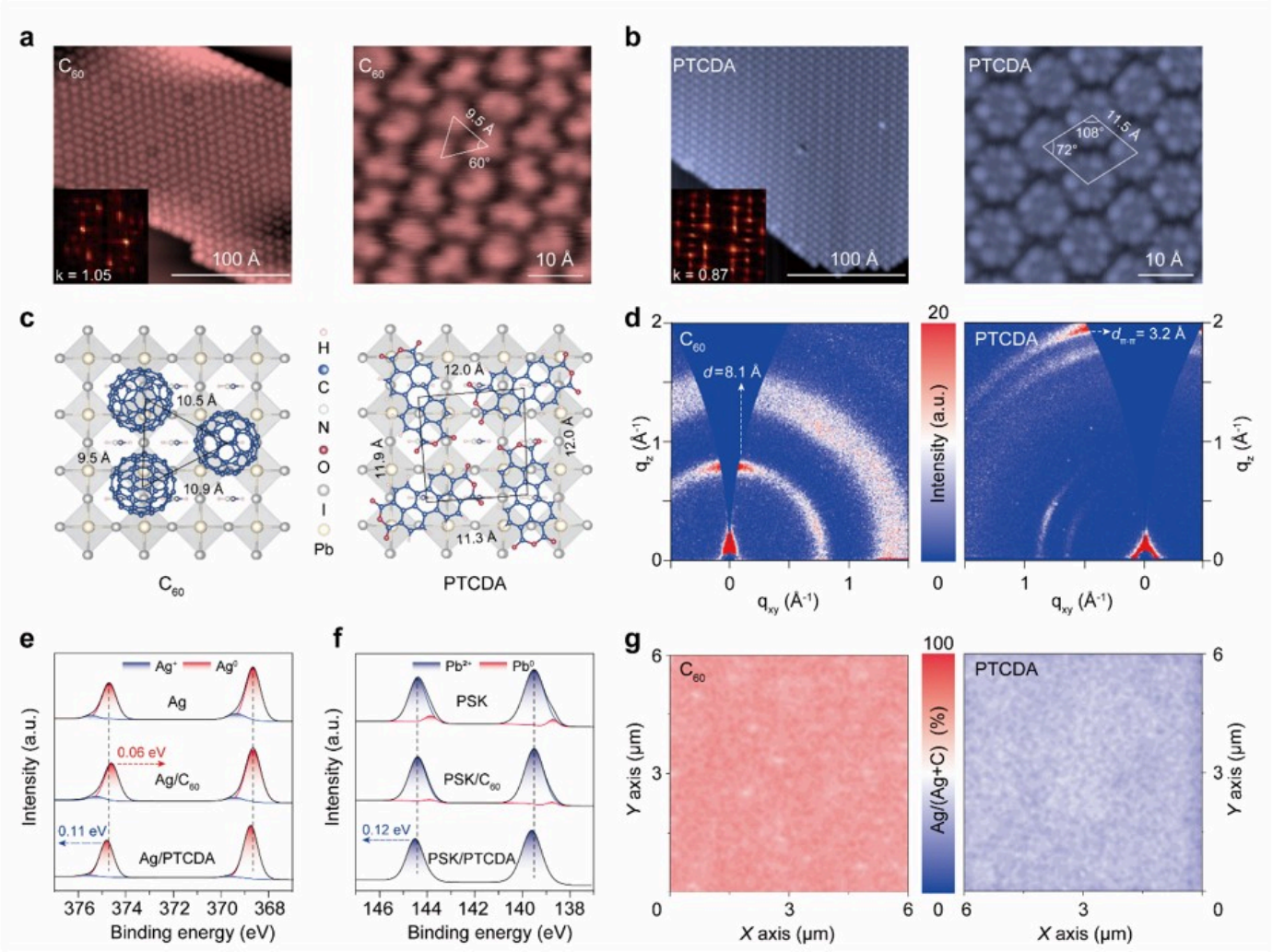


Figure 1

Structural ordering and surface properties of self-assembled molecules. (**a, b**) High-resolution STM images of self-assembled C_{60} and PTCDA on Ag(111) at 77 K. (**a**) C_{60} images were acquired at scan sizes of 20 nm × 20 nm (0.9 V, 74 pA; inset: FFT pattern) and 4.8 nm × 4.8 nm (1.5 V, 110 pA). (**b**) PTCDA images were acquired at 20 nm × 20 nm (1.0 V, 110 pA; inset: FFT pattern) and 4.8 nm × 4.8 nm (–0.3 V, 75 pA). (**c**) Simulated repeating units of C_{60} and PTCDA on the $FAPbI_3$ (100) surface, arranged in triangular and square lattices, respectively. (**d**) GIWAXS patterns of C_{60} and PTCDA, with characteristic scattering features corresponding to vertical molecular spacings of ~8.1 Å and ~3.2 Å, respectively. (**e**) XPS Ag 3*d* spectra of pristine Ag, C_{60}/Ag, and PTCDA/Ag. (**f**) XPS Pb 4*f* spectra of pristine PSK, PSK/C_{60}, and PSK/PTCDA. (**g**) AES maps of the Ag/(Ag + C) atomic ratio for Ag/C_{60} and Ag/PTCDA.

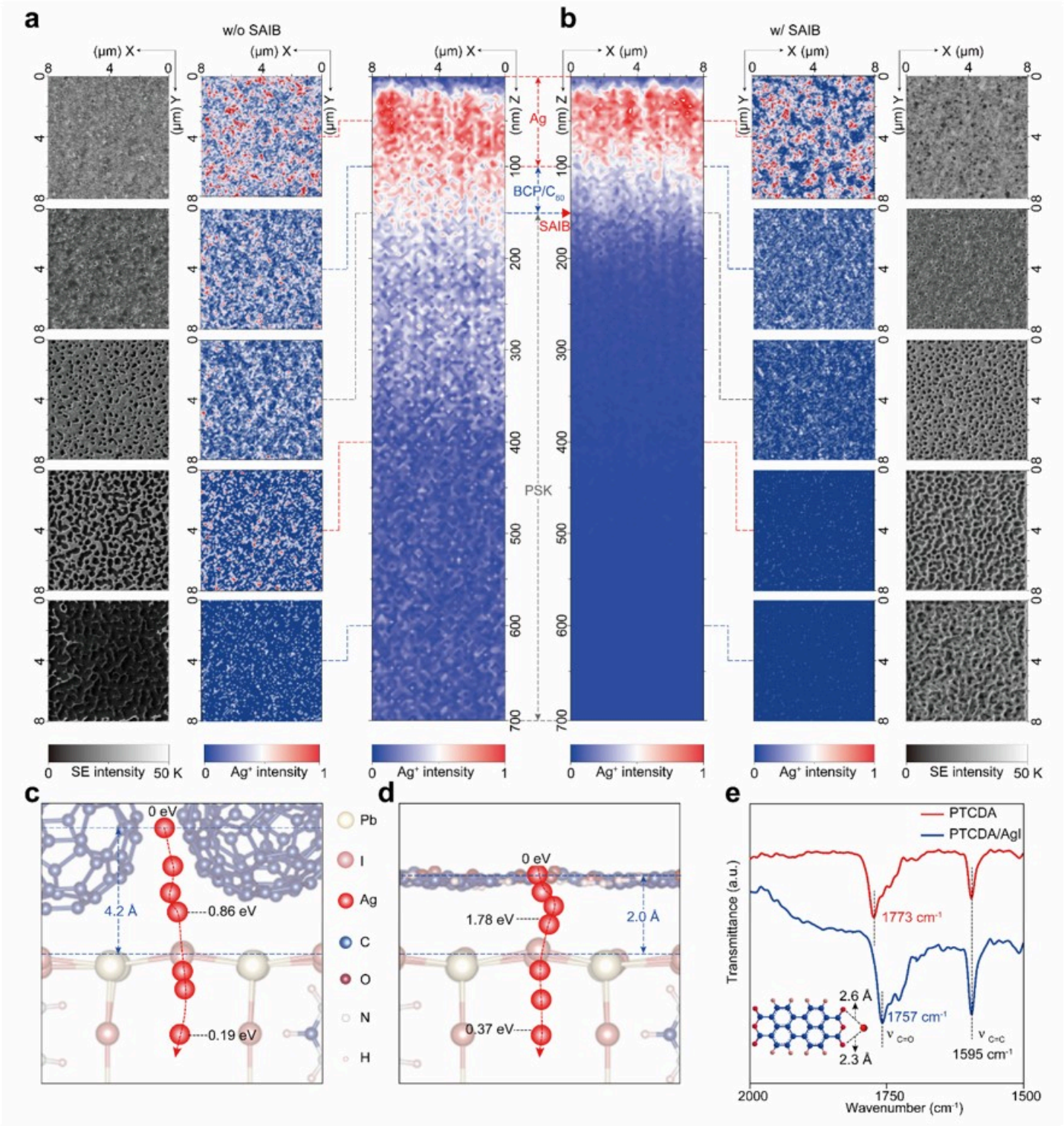


Figure 2

A coordinative network encircling each molecule as an ion barrier. (**a, b**) ToF-SIMS depth profiling of Ag^+ distribution in w/o SAIB (**a**) and w/ SAIB (**b**) PSCs after 72 h of MPPT operation. Side columns show top-view Ag^+ distribution maps (from five depths: 50, 100, 150, 400, and 600 nm) and corresponding SEM images. (**c, d**) Simulated Ag^+ migration pathways through the repeating units of C_{60} (**c**) and PTCDA (**d**) toward the $FAPbI_3$ (100) surface. (**e**) FTIR spectra of pristine PTCDA and PTCDA/AgI films.

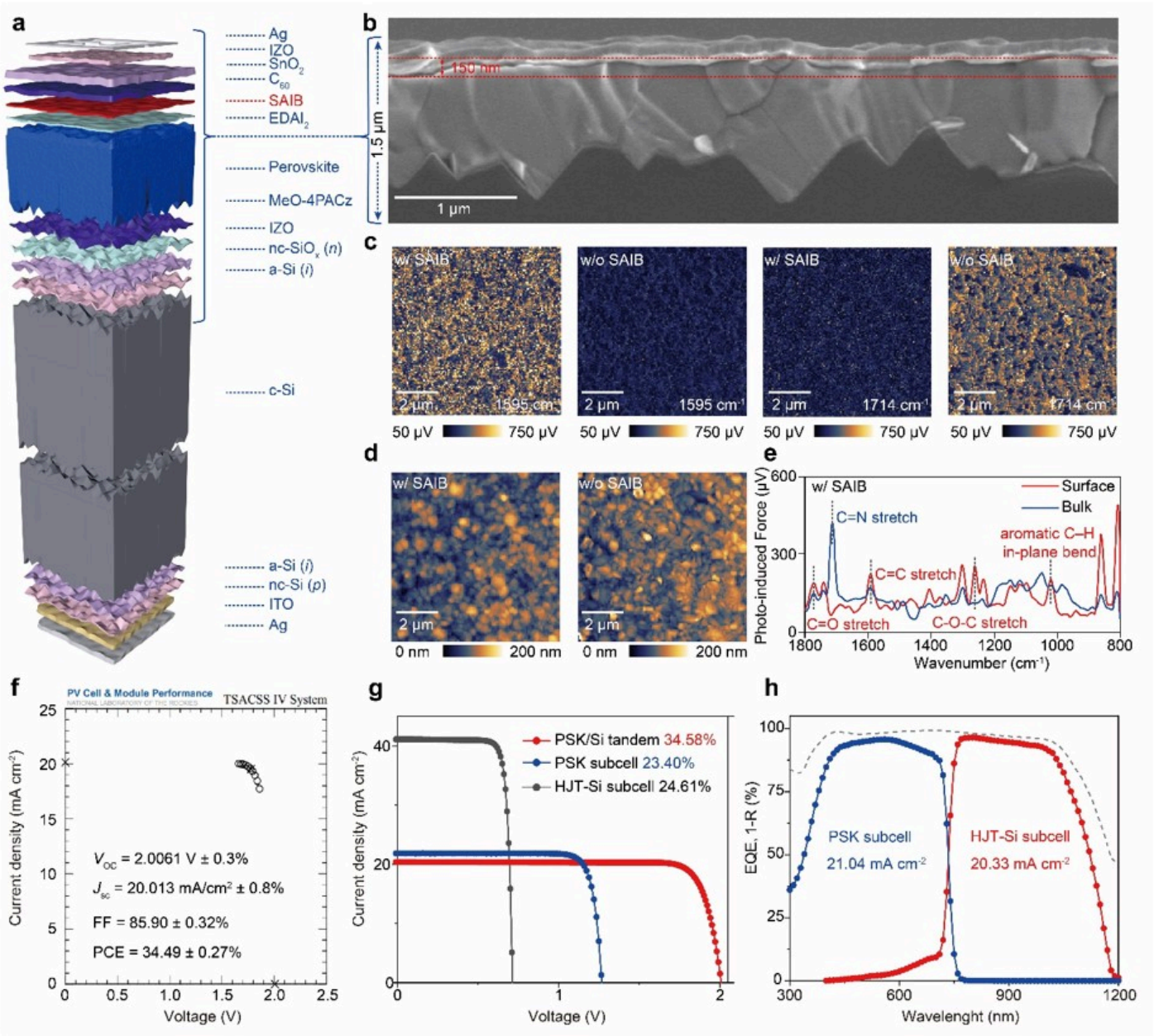


Figure 3

Conformal SAIB coating on textured silicon and tandem performance. (**a**) Schematic of the PSK/HJT-Si tandem device structure. (**b**) Cross-sectional SEM image of the tandem device (upper portion). (**c**) PiFM chemical mapping at 1595 cm^{-1} (C=C stretch from PTCDA) and 1714 cm^{-1} (C=N stretch from PSK) for w/ and w/o SAIB samples. (**d**) PiFM surface morphology mapping (non-contact mode) of w/ and w/o SAIB samples. (**e**) Depth-resolved PiIR spectroscopy of the w/ SAIB sample at the top surface and in the bulk. (**f**) NREL-certified steady-state efficiency of the PSK/HJT-Si tandem (elapsed time: 619 s). (**g**) *J–V* curves of the Si subcell (gray), PSK subcell (blue), and PSK/Si tandem cell (red). **(h)** EQE spectra of the PSK top and Si bottom subcells.

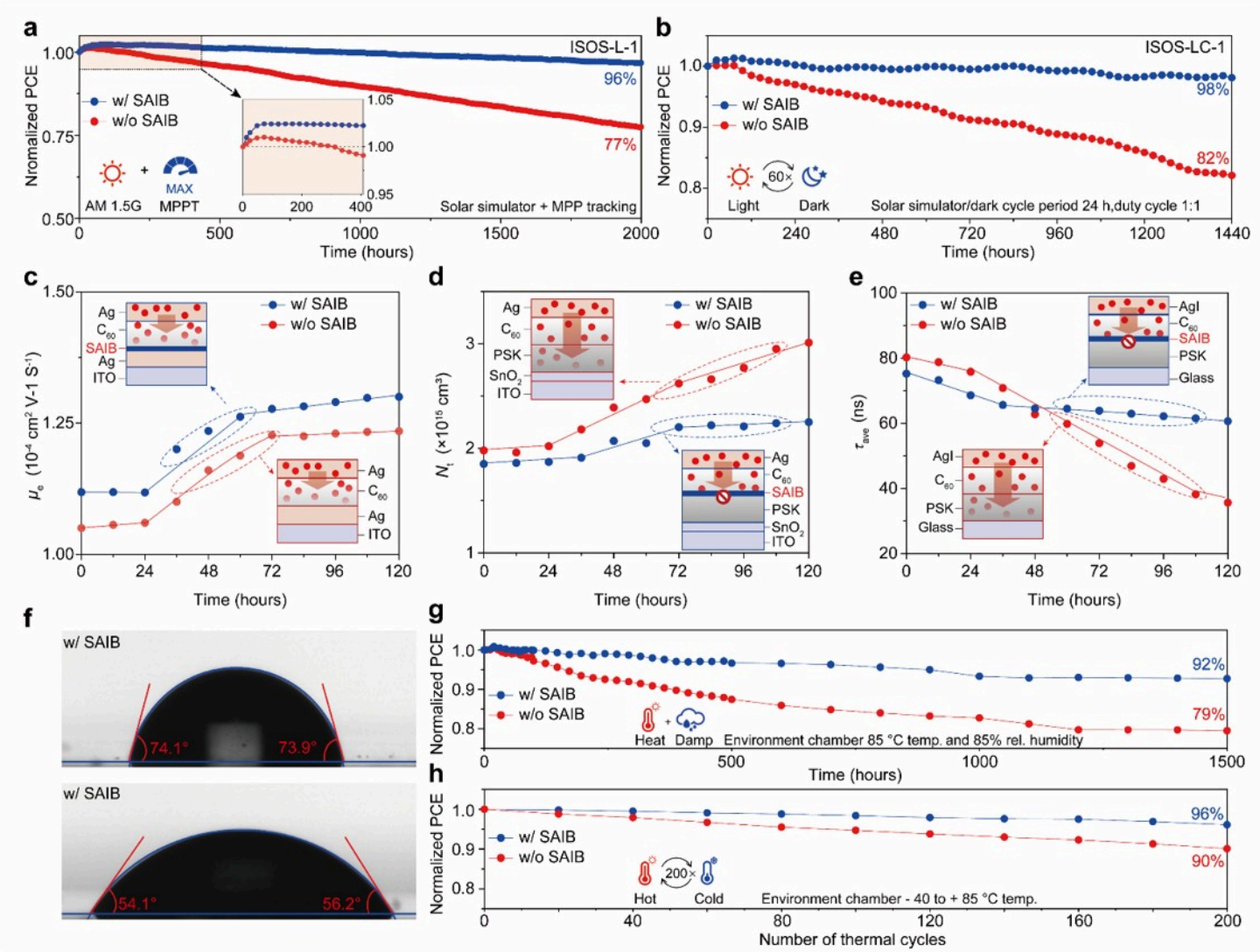


Figure 4

Resolving the efficiency rise-and-decay phenomenon and device stability. (**a, b**) Normalized PCE evolutions of w/ and w/o SAIB tandems with encapsulation under continuous MPPT (**a**, 1-sun illumination, ISOS-L-1) and light-dark cycling (**b**, 24-h cycle, 1:1 duty cycle, ISOS-LC-1). (**c–e**) μ_e, N_t, and τ_{ave}derived from SCLC and TRPL analyses of w/ and w/o SAIB samples during 120 h of continuous illumination. Device structures: (**c**) glass/ITO/Ag/SAIB (w/ or w/o)/C_{60}/Ag; (**d**) glass/ITO/SnO_2/PSK/SAIB (w/ or w/o)/C_{60}/Ag; (**e**) glass/PSK/SAIB (w/ or w/o)/ C_{60}/AgI. (**f**) Static water contact-angle images of w/o and w/ SAIB PSK top surfaces. (**g, h**) Normalized PCE evolutions of w/o and w/ SAIB tandems under damp-heat (**g**, 85 °C, 85% RH, ISOS-D-3) and thermal shock (**h**, −40 to 85 °C, 10 °C min^{-1} ramps, 30 min per cycle, ISOS-T-3).

Supplementary Files

This is a list of supplementary files associated with this preprint. Click to download.

- NatureEnergySupplementaryInformationDBPR.docx